

Characterization of Transition to Detachment of Magnetic Confinement Plasmas via Data Driven Approach in LHD

Yugo ISOBE¹⁾, Hiroshi YAMADA^{1)*}, Tatsuya YOKOYAMA²⁾,
Masahiro KOBAYASHI^{1,3)}, Yasuhiko IGARASHI⁴⁾, Yoshiro NARUSHIMA^{3,5)},
Yuki TAKEMURA^{3,5)}, Chihiro SUZUKI^{3,5)}, Ryuichi SAKAMOTO^{3,5)}

¹⁾ Graduate School of Frontier Sciences, The University of Tokyo, Kashiwa, Chiba 277-8561, Japan

²⁾ National Institutes of Quantum Science and Technology, Naka 311-0193, Japan

³⁾ National Institute for Fusion Science, National Institutes of Natural Sciences, Toki 509-5292, Japan

⁴⁾ Tsukuba University, Tsukuba 305-8573, Japan

⁵⁾ The Graduate University for Advanced Studies, SOKENDAI, Toki 509-5292, Japan

(Received 13 November 2024 / Accepted 26 January 2025)

The transition condition from an attached state to a detached state of magnetic confinement plasmas has been investigated by a data-driven approach in LHD. This transition is defined as a binary classification problem of two states, and Support Vector Machine together with Exhaust Search has been applied. The boundary between detachment and attachment in the physical parameter space has been identified as a decision function comprising radiation and heating power, magnetic field and the resonant magnetic flux. While resonant magnetic perturbation (RMP) secures stable detached plasmas, it has been found that the featured parameter is not externally applied RMP itself but the plasma response to RMP. The present approach gives a robust separation boundary even for the extended operation with radiation enhancement by neon gas puff. Anomaly detection with a singular value decomposition has been also applied to the temporal behavior and identified pre- and post-relationships of each physical parameter in time. Emissions from carbon impurities with low ionization potential start to change prior to the RMP penetration and then the drop of ion saturation current, that is the transition to detachment, happens. These temporal sequences do not necessarily mean causality but are helpful for approach to physical inference.

© 2025 The Japan Society of Plasma Science and Nuclear Fusion Research

Keywords: detached plasma, resonant magnetic perturbation, large helical device, support vector machine, anomaly detection

DOI: 10.1585/pfr.20.1402024

1. Introduction

Mitigation of divertor heat load is one of the most critical issues in the development of a magnetic fusion reactor. Among a variety of ideas to resolve this issue, the plasma operation detached from the divertor plate is a promising approach. Detached plasma reduces the heat flux reaching the divertor target plate and consequently helps avoidance of melting and mitigation of thermal stress and sputtering. Detachment is driven by enhanced dissipation of energy through interaction between plasma in particular impurity ions and neutrals [1, 2]. While the heat flux onto the divertor is dramatically suppressed under the detached plasma condition, plasma often tends to be thermally unstable easily due to enhanced radiation. Propagation of cold front from the divertor to the core region must be controlled to avoid radiation

collapse. In the experiment on the Large Helical Device (LHD), the detached plasma was successfully sustained stably by applying $m/n = 1/1$ Resonant Magnetic Perturbation (RMP) [3–5]. This resonant surface is located in the edge region. The remnant island structure created by this RMP in the stochastic magnetic boundary secures detached plasma with preventing radiation collapse. A series of studies have indicated that selective cooling around the peculiar magnetic structure plays an essential role, however, the transition condition has not been identified quantitatively yet. Identification of what plasma parameters contribute to the occurrence of detached plasma is expected to lead to the establishment of operational control of stable detached plasmas and understanding of the underlying physics.

Detachment is a consequence of complex and compound physical dynamics including transport, stability and atomic processes. Numerical simulations of EMC3-EIRENE [6] have qualitatively reproduced the radiation distribution

*Corresponding author's e-mail: yamada.hiroshi@k.u-tokyo.ac.jp

during detached phase with RMP as compared with imaging bolometer measurements while the radiative power intensity was found to be overestimated by the simulation [7]. The radiated power of the numerical simulation tends to be closer to that of experiments with increased cross-field transport coefficient. Dynamics of the detachment transition was analyzed with originally developed 2-D time-dependent transport code [8] and it was found that the X-point of the island facilitates the impurity radiation to drive detachment transition. Numerical analysis taking into account the magnetic island structure pointed out an important role of the island flux tubes at the O-point to avoid penetration of the radiation layer into the confinement region [9]. In contrast to a-priori modelling approach like these numerical simulations based on modeled differential equations, a data-driven a-posteriori approach has been taken in this study. The question is whether statistical characteristics derived from existing data has a capability to predict occurrence of detachment in a specific plasma discharge or not. Here Support Vector Machine (SVM) and Exhaustive Search (ES) [10] were used to build a predictor. SVM is one of supervised machine learning methods and classifies two states. ES is useful for a sparse modeling by identifying featured parameters. It has been already demonstrated that this methodology of ES-SVM works well in predicting abrupt termination events such as tokamak plasma disruption [11] and radiation collapse in a helical system [12]. It is noted that the present methodology by means of ES-SVM relies on the assumption that the state at the specific time slices is a basis of temporal evolution in the future other than some time derivatives. Therefore time derivatives of physical quantities are not included in the analysis.

2. Experiment

The data from NBI heated plasmas in LHD has been compiled to the dataset and analyzed. The magnetic configuration was fixed to the case with the magnetic axis position R_{ax} of 3.9 m, where the $m/n = 1/1$ resonance is located in the stochastic boundary layer. Figure 1 shows typical waveforms of the plasma discharge with the transition from attachment to detachment. By ramping up density, radiation power increases gradually. Then the detachment is clearly identified by an abrupt drop in the ion saturation current I_{sat} , namely ion flux onto the divertor plate. In the magnetic configuration studied here, the divertor particle flux channel width is about or less than 2 cm, which is resolved with three divertor probe tips. At the detachment transition, the particle flux decreases at all the three probe tips. The flux shown in Fig. 1 is summed values over all probe tips. The change in I_{sat} occurs in the time scale of 10 ms and this drop is very clear. Therefore, the data can be labelled as attachment and detachment according to the signal of I_{sat} .

Four operational parameters of magnetic field B , RMP coil current I_{RMP} , line averaged density \bar{n}_e and absorbed heating power P_{abs} have been scanned in wide ranges to reduce correlation between these parameters in the experiment. The

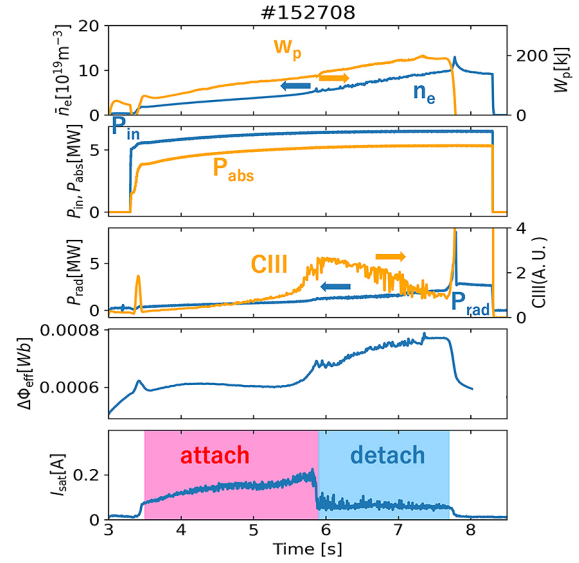


Fig. 1. Waveforms of a typical plasma discharge with detachment transition. Top panel: line averaged electron density \bar{n}_e and stored energy W_p , the second panel: input heating power P_{in} and absorbed heating power P_{abs} , the third panel: radiation power P_{rad} and C III emission intensity, the fourth panel: perturbed magnetic flux of plasma response $\Delta\Phi_{eff}$, bottom panel: ion saturation current onto the divertor target plate I_{sat} . Detachment transition occurs at 5.9 s.

RMP coil current reaches a steady value 1 s before the start of plasma discharges and is kept constant during the plasma discharge. The absorbed NBI heating power has been evaluated by the numerical code FIT3D [13]. Other than four operational parameters, 10 potential featured parameters characterizing plasma have been selected from available measurement (see Table 1). They are plasma β_{dia} evaluated by diamagnetic loop measurement, hydrogenic isotope ratio $n_D/(n_H + n_D)$ evaluated by passive spectroscopy, and radiation power fraction P_{rad}/P_{abs} , in the first place. Low to medium-Z line emissions are pronounced in edge plasma and emissions of C III, C IV, O V, O VI and Fe XVI with different ionization potentials are incorporated in the dataset. Also the amplitude of $m/n = 1/1$ perturbed magnetic flux $\Delta\Phi_{eff}$ as a plasma response to the RMP, which reflects the generated island width, attracts interest together with its phase θ_{eff} . These are evaluated from the measurement of the flux-loop array [14]. Since the plasma often shields or amplifies the externally applied RMP, it should be noted that the real change of magnetic topology is not exactly the same as externally applied RMP. Table 1 summarizes the parameter ranges in the dataset. The dataset has been compiled with 14 parameters in total and the labels of detachment and attachment.

The timing of detachment, that is the transition from attachment to detachment, is defined by the maximum time rate of change of the signal of ion saturation current I_{sat} during the dropping phase. It should be noted that the data is taken from the phases from 0.2 s to 0.1 s before the transition for attachment and from 0.1 s to 0.2 s after the transition for detachment, respectively. This means data in the vicinity of

Table 1. Parameters compiled in the dataset. Parameters 1–4 are operational parameters and parameters 5–14 are resultant observations in the experiment.

parameters	range	units
1. Magnetic field B	1.36, 2.54	T
2. RMP coil current I_{RMP}	0–3340	A
3. Line averaged density \bar{n}_e	1.74–10.5	10^{19} m^{-3}
4. Absorbed heating power P_{abs}	2.18–6.44	MW
5. Plasma beta β_{dia}	0.10–0.82	%
6. Isotope ratio $n_D/(n_H + n_D)$	0.01–0.56	—
7. Radiation power fraction P_{rad}/P_{abs}	0.10–0.63	—
8–12. Impurity line emissions (C III, C IV, O V, O VI, Fe XVI)	—	AU
13. Resonant perturbed flux $\Delta\Phi_{eff}$	0.12–7.47	10^{-4} Wb
14. Resonant perturbed phase θ_{eff}	0–1.71	rad.

the transition in time ± 0.1 s is screened out since some peculiar temporal behavior like a spike appearing at the transition, which could mislead binary classification.

3. Identification of Transition Condition from Attached Plasma to Detached Plasma

It is already empirically known that the detachment tends to occur in the high density regime since $P_{rad} \propto \bar{n}_e^2$. Figure 2 shows the histogram of two states along the class of the line averaged electron density from the dataset. Indeed, the detachment state is distributed in the higher density regime, however, the significant overlap of distributions of detachment and attachment indicates that other plasma parameters play roles for the transition through their combination.

In line with the ES-SVM scheme, the classification performance has been compared by changing the number of parameters in the combination among 14 parameters. The kernel of SVM used here is linear. It should be noted that the logarithmic values of parameters are used in the analysis since it is desirable to get the power law expression for the hyper plane to separate attachment and detachment. The performance is assessed in terms of F1-score. The F1-score is the harmonic mean between the precision and the recall and the index how the positive class is detected accurately and the negative class is not detected falsely. The result is summarized in Fig. 3. The right diagram shows the best combination of each case with the numbers (K) of parameters. The color bar corresponds to the weight. While there is replacement of key parameters depending on their combination, as seen in the right diagram, line averaged density \bar{n}_e , magnetic field B , and the perturbed flux $\Delta\Phi_{eff}$ are included in the top combinations regardless of K . The left diagram shows the best F1-score for each K and it can be seen that the classification performance saturates at $K = 3$. Therefore, three parameters of \bar{n}_e , B , and $\Delta\Phi_{eff}$ are relevant as the key parameters of the transition condition between attachment and detachment.

The hyperplane to classify these two states is given by

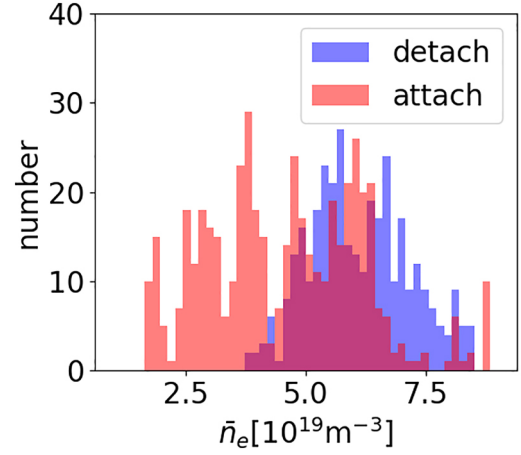
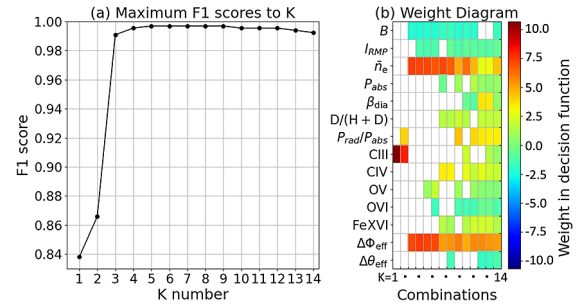


Fig. 2. Frequency distribution of detachment in blue and attachment in red along the class of the line averaged density.


 Fig. 3. Summary of results from ES-SVM for the dataset without Ne puff. The left graphs shows the best F1-scores for each K . The right diagram shows the parameters included in each combination plotted in the left graph. The color bar corresponds to the weight of each parameter.

$$e^{15.2} \bar{n}_e^{4.1} B^{-3.7} \Delta\Phi_{eff}^{2.3} = 1. \quad (1)$$

The data distribution is shown on the plane of $\Delta\Phi_{eff}$ and other remaining function in Fig. 4. The solid line is the cross-section of the hyperplane give by Eq. (1). The two states of attachment and detachment are clearly separated (here look at only solid circle symbols for a while). The F1-score is 0.991. The cases with intentional neon (Ne) puff, which were not included in this analysis, are also plotted in crosses and these will be discussed later. Here, it should be noted that the perturbed flux $\Delta\Phi_{eff}$ is chosen rather than the RMP current I_{RMP} . The RMP current is not regarded as a key parameter and indeed intentional incorporation of the RMP current into the combination with \bar{n}_e , B and $\Delta\Phi_{eff}$ shows that transition condition does not depend on I_{RMP} . The result in Fig. 4 indicates the threshold of $\Delta\Phi_{eff}$ depends on density and magnetic field. The reason why $\Delta\Phi_{eff}$ is chosen rather than I_{RMP} can be clarified in Fig. 5 showing $\Delta\Phi_{eff}$ as a function I_{RMP} . The cases with detachment in blue exhibits a clear proportionality between $\Delta\Phi_{eff}$ and I_{RMP} . However, the perturbed flux $\Delta\Phi_{eff}$ is suppressed in the cases with attachment in red. This means that plasma shields the penetration of RMP when plasma is attached. This property agrees with the

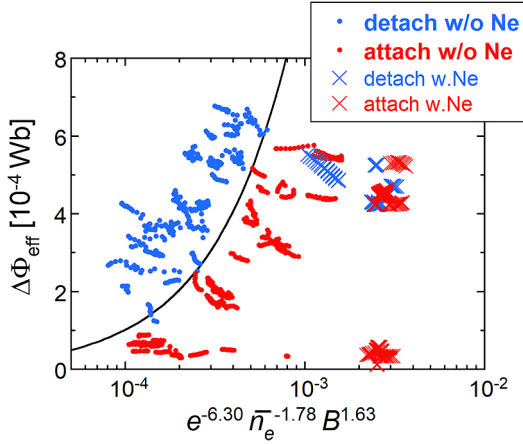


Fig. 4. Classification of attached state in red and detached state in blue. The boundary shown in a solid curve is given by the decision function Eq. (1) corresponding to only the case without Ne puff. Solid symbols are cases without Ne puff and crosses are cases with Ne puff.

observation in the previous study [15] that suggested the detachment takes place with penetration of RMP.

Plasma detachment can be eased by enhanced radiation with intentional impurity neon puff [16]. Supplements of the cases with Ne puff are plotted in Fig. 4. It can be seen that detachment occurs in the attachment region identified by the analysis of the cases without Ne puff. Ne puff facilitates detachment in the lower density regime and the boundary given by Eq. (1) is not applicable to the cases with Ne puff. Then the ES-SVM analysis has been reexamined for the extended dataset including the cases with Ne puff. The line emission from Ne VIII is added to analyzed parameters. The resultant identified classification function is

$$e^{16.1} P_{abs}^{2.9} (P_{rad}/P_{abs})^{4.2} B^{-2.5} \Delta\Phi_{eff}^{1.5} = 1. \quad (2)$$

The perturbed magnetic flux $\Delta\Phi_{eff}$ and the magnetic field B remain as key parameters while the line averaged density \bar{n}_e is replaced by the absorbed power P_{abs} and radiation power fraction P_{rad}/P_{abs} . Figure 6 shows the data distribution on the plane of $\Delta\Phi_{eff}$ and the remaining function. The separation performance by Eq. (2) for the cases both with and without Ne puff degrades a little bit in comparison with Eq. (1) for the cases only without Ne puff (F1-scores are 0.991 and 0.958 for the cases without Ne puff in Fig. 4 and the cases both with and without Ne puff in Fig. 6, respectively). It should be noted that the boundary given by Eq. (1) is not relevant to the cases with Ne puff and that the separation performance by Eq. (2) remains at high level for all cases. Therefore, Eq. (2) is more robust expression for attachment/detachment bifurcation than Eq. (1).

4. Anomaly Detection

The ES-SVM analysis yields the expression of hyper-plane to classify two states; attachment and detachment. It is reminded that this analysis does not consider any temporal

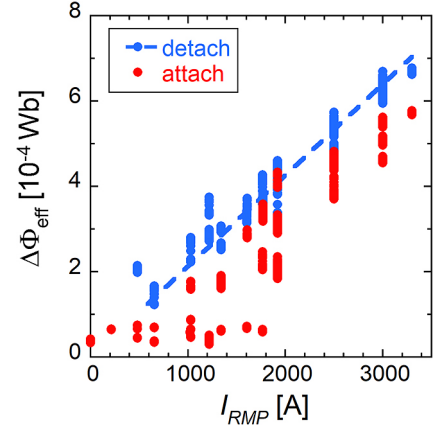


Fig. 5. Comparison of perturbed resonant flux $\Delta\Phi_{eff}$ with RMP coil current I_{RMP} . Red and blue symbols are the cases of attached plasma and detached plasma, respectively.

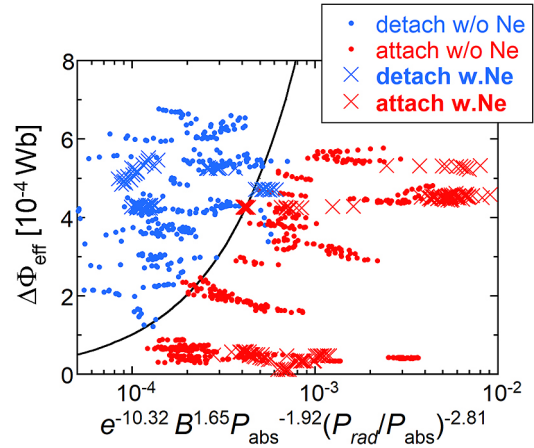


Fig. 6. Classification of attached state in red and detached state in blue. The boundary shown in a solid curve is given by the decision function Eq. (2). Solid symbols are cases without Ne puff and crosses are cases with Ne puff.

changes. In a broad sense, it assumes so to the ergodic hypothesis that the average in long time matches the average in the phase space. In this regard, the result from the ES-SVM analysis can tell the correlation in the phenomena between parameters but not causality.

In order to look into temporal behavior, which would be a hint for causality, the anomaly detection based on the singular-spectrum transformation (SST) has been applied. The basics and the procedure of SST are described in ref. [17, 18]. A trajectory matrix containing the information in the past $\mathbf{X}^{(t)}$ and a test matrix containing the information in the vicinity of the present time (or the time of interest) $\mathbf{Z}^{(t)}$ are configured from time series data with the time window of 90 ms and the lag time of 100 ms. Then the corresponding matrices of left singular vectors $\mathbf{U}_r^{(t)}$ and $\mathbf{Q}_m^{(t)}$, which exhibit a characteristic pattern, are obtained by singular value decomposition (SVD) of these trajectory matrix and the test matrix. Discrepancy between $\mathbf{U}_r^{(t)}$ and $\mathbf{Q}_m^{(t)}$ indicates the change of a pattern. The change score defined by $1 - \|\mathbf{U}_r^{(t)T} \mathbf{Q}_m^{(t)}\|$ is an index of anomaly used here. The temporal order of emer-

gence of anomaly in each signal gives the pre- and post-relationships between parameters and suggests a clue to build a conjecture towards causality.

Figure 7 shows the temporal changes of the change score for parameters characterizing plasma discharges. These are the conditional averages of 30 discharges in the case without Ne puff, where the transition timing is matched for synchronization. The temporal change of the decision function given by the left hand side of Eq. (1), which is an index of proximity to detachment, is also shown. Variation in each case is not smoothed out by the averaging process and common characteristic behaviors are rather pronounced, which suggests the existence of a physical pattern in temporal behavior in transition from attachment to detachment.

The histogram is the appearance frequency of the largest change score of each parameter in the interested time window (± 0.3 s from the transition time shown in Fig. 7).

The change of impurity line emissions with low ionization potential (C III(48 eV) and C IV(65 eV)) appears first and then radiation and density change. These changes are seen before the decision function reaches 1. The perturbed magnetic flux $\Delta\Phi_{eff}$ starts to change next. The anomaly in I_{sat} that is the transition from attachment to detachment appears at the same time as settling down of $\Delta\Phi_{eff}$, which reflects completion of RMP penetration. These changes happen immediately after the decision function exceeds 1. The line emissions from relative high ionization potential follow after the transition together with secondary change in the line averaged density and radiation power. The secondary appearance of anomaly in emissions of C III and C IV is supposed to be attributed to the consequence of detachment. The emissions with rather high ionization potential, O V(114 eV) and O VI(138 eV), do not show any anomaly before the transition, but they change after the transition. These change of impurity emissions reflect the change of the volume and density of the domain with the specific electron temperature. Simulation study of EMC3-EIRENE has suggested that radiation loss by line emissions from carbon is important for detachment [7], while the analysis of dynamic behavior has not been feasible because EMC3-EIRINE is a time-independent code. The results of the present anomaly detection, particularly on the dynamic behavior of the detachment transition, provide important physical insight for further understanding of detachment mechanism.

5. Conclusions

The transition condition from attachment to detachment in NBI heated plasmas in LHD has been identified as a decision function by means of ES-SVM. This study owes the earlier achievement that established stable detached plasma operation with RMP. The decision function consists of 4 featured parameters; the absorbed heating power, radiation power fraction, magnetic field and the perturbed $m/n = 1/1$ magnetic flux including plasma response. This decision function gives the boundary hyperplane to separate two states

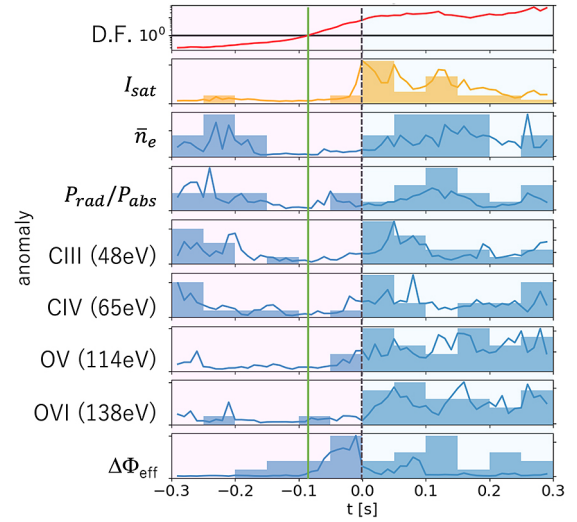


Fig. 7. Temporal changes of the decision function value and change scores (indices of anomaly) of featured parameters. The abscissa is the time difference from the detachment transition. The dotted and solid vertical lines are the times when the transition to detachment is identified and decision function (the left hand side of Eq. (1)) reaches 1, respectively.

(attachment and detachment) in this four dimensional space. Capability of separation is almost perfect with F1-score of 0.958 including the case of enhanced radiation with Ne puff. It should be noted here that the perturbed flux is chosen as a key parameter rather than the RMP coil current. This means that plasma tends to shield the externally applied RMP, in particular when the plasma is attached and that the actual change of magnetic topology as consequence of plasma response to the externally applied RMP is essential.

Although classification of attachment and detachment by ES-SVM is successful, this result indicates the correlation between parameters but not causality. The temporal change of time series data is discussed in terms of emergence of anomaly. Here quantification of pattern change by means of SST with SVD has been applied. Emissions from carbon impurities with low ionization potential change before the decision function reaches 1 (identified boundary). Then RMP penetration starts and the drop of ion saturation current, that is the transition to detachment, happens at the same time of completion of RMP penetration. Time dependent simulation of edge plasma in 3-D plasma and magnetic field geometry is challenging since complex physical processes are interlinked. The observed temporal order of physical quantities suggests a hint for a conjecture of detachment dynamics and deliberation combined with even the time independent computation by EMC3-EIRENE will be a valuable future work.

Acknowledgments

The authors are grateful to the excellent technical support by the LHD experiment group, and the Department of Engineering and Technical Services at the National Institute for Fusion Science. This work was partly supported by the

JSPS Grant-in-Aid for Scientific Research 20K20426 and the NIFS grant NIFS24KIPS007. The data supporting the findings of this study are available in the LHD experiment data repository at <https://doi.org/10.57451/lhd.analyzed-data>.

- [1] P.C. Stangeby, *Plasma Phys. Control. Fusion* **60**, 044022 (2018).
- [2] S.I. Krashennikov and A.S. Kukushkin, *J. Plasma Phys.* **83**, 155830501 (2017).
- [3] M. Kobayashi *et al.*, *Nucl. Fusion* **53**, 093032 (2013).
- [4] M. Kobayashi *et al.*, *Nucl. Fusion* **59**, 096009 (2019).
- [5] M. Kobayashi *et al.*, *Nucl. Fusion* **62**, 056006 (2022).
- [6] Y. Feng *et al.*, *Contrib. Plasma Phys.* **54**, 426 (2014).
- [7] S.N. Pandya *et al.*, *Nucl. Fusion* **56**, 046002 (2016).
- [8] M. Kobayashi and M.Z. Tokar, *Contrib. Plasma Phys.* **60**, e201900138 (2020).
- [9] M.Z. Tokar and M. Kobayashi, *Plasma Phys. Control. Fusion* **62**, 085011 (2020).
- [10] Y. Igarashi *et al.*, *J. Phys: Conference Series* **1036**, 012001 (2018).
- [11] T. Yokoyama *et al.*, *Plasma Fusion Res.* **16**, 1402073 (2021).
- [12] T. Yokoyama *et al.*, *J. Fusion Energy* **39**, 500 (2020).
- [13] R. Seki *et al.*, *Plasma Fusion Res.* **14**, 3402126 (2019).
- [14] Y. Narushima *et al.*, *Plasma Fusion Res.* **8**, 1402058 (2013).
- [15] Y. Narushima *et al.*, *Nucl. Fusion* **48**, 075010 (2008).
- [16] K. Mukai *et al.*, *Nucl. Fusion* **61**, 126018 (2021).
- [17] V. Moskvina and A. Zhigljavsky, *Communications in Statistics-Simulation and Computation* **32**, 319 (2003).
- [18] T. Ide and K. Tsuda, in *Proc. 2009 SIAM International Conference on Data Mining, SDM 09*, (Sparks, Nevada, USA, 2009), 97–108.